

1

Nanoscale Metallo-Dielectric Coherent Light Sources

Maziar P. Nezhad, Aleksandar Simic, Amit Mizrahi, Jin-Hyoung Lee, Michael Kats, Olesya Bondarenko, Qing Gu, Vitaliy Lomakin, Boris Slutsky, and Yeshaiahu Fainman

1.1

Introduction

Compact photonic components are important for the design and fabrication of integrated optical devices and circuits. In the case of light sources, reducing the size can result in improved metrics such as higher packing density and reduced power consumption and also may enhance cavity–emitter interactions such as the Purcell effect. Until recently it was commonly known that the minimum size for a laser is ultimately determined by the free-space wavelength, λ_0 . For example, as the size of a conventional Fabry–Perot semiconductor laser is scaled down in all three dimensions toward λ_0 , three effects adversely influence the lasing process. Firstly, the roundtrip path of the optical wave in the gain medium is shortened. Secondly, radiative losses from the end mirrors have an increased effect. Thirdly, the lateral field confinement in the resonator waveguide is reduced, resulting in a smaller overlap of the optical mode with the gain medium. All these effects lead to a significant increase in the lasing threshold. As a result lasing cannot be achieved below a certain size limit. By allowing the laser size to increase in one or two dimensions, it is possible to reduce the physical size of the laser in the remaining dimension(s) to values below this limit. For example, the disk thickness in whispering-gallery-mode (WGM) lasers [1] can be reduced to a fraction of the free-space wavelength [2] but, to compensate for the small thickness, the disk diameter must be increased. It should be noted that, in addition to the optical mechanisms noted above, nonradiative surface recombination can have a non-negligible negative effect on the emitter efficiency and thus needs to be accounted for in the design and analysis of such sources. The ultimate challenge in this respect is concurrent reduction of the resonator size in all three dimensions, and, at the same time, satisfying the requirements for lasing action.

The size of an optical cavity can be defined using different metrics, for example, the physical dimensions of the cavity or the size of the optical mode. However, if the goal of size reduction is to increase the integration density (for example, in a

laser array), the effective cavity size should account for both the overall physical dimensions of the resonator and the spread of the optical mode beyond the physical boundary of the resonator. By this token, most conventional dielectric laser cavities are not amenable to dense integration because they have either a large physical footprint or a large effective mode. For example, distributed Bragg resonators [3] and photonic-crystal cavities [4] (both of which can be designed to have very small mode volumes) have physical footprints that are many wavelengths in size, due to the several Bragg layers or lattice periods that are required for maintaining high finesse. On the other hand, it has been demonstrated that the diameter of thick (λ_0/n) micro-disk lasers can be reduced below their free-space emission wavelength [5]; however, the spatial spread of the resultant modes (which have low azimuthal numbers owing to the small disk diameters) into the surrounding space beyond the physical boundaries of the disks may lead to mode coupling and formation of “photonic molecules” in closely spaced disks [6]. For illustration purposes, an $M = 4$ WGM for a semiconductor disk with radius $r_c = 460$ nm and height $h_c = 480$ nm (Figure 1.1a) is shown in Figure 1.1b, clearly indicating the radiative nature of the mode and its spatial spread, which, as mentioned, can lead to mode coupling with nearby structures. (M is the azimuthal order of the resonance, corresponding to half the number of lobes in the modal plot of $|E|$.)

One approach to alleviate these issues is to incorporate metals into the structure of dielectric cavities, because metals can suppress leaky optical modes and effectively isolate them from their neighboring devices. The modes in these metallo-dielectric cavities can be grouped into two main categories: (i) surface bound (that is, surface

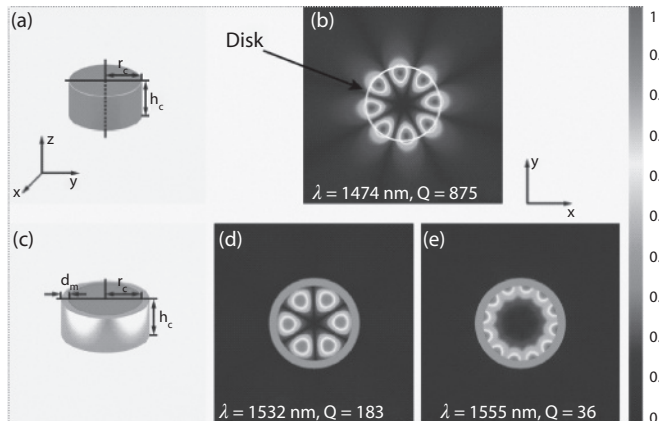


Figure 1.1 The $M = 4$ whispering gallery resonance for a thick semiconductor disk (a) is shown in (b) ($r_c = 460$ nm, $h_c = 480$ nm, and $n_{\text{semi}} = 3.4$). Note the spatial spread of the mode compared to the actual disk size. (c) The same disk encased in an optically thick ($d_m = 100$ nm) gold shield will have

well-confined reflective (d) and plasmonic (e) modes but with much higher mode losses. $|E|$ is shown in all cases and the section plane is horizontal and through the middle of the cylinder. (From [7].) (Please find a color version of this figure on the color plates.)

plasmon polariton (SPP) resonant modes and (ii) conventional resonant modes (called *photonic modes*), resulting purely from reflections within the metal cavity. Although they are highly confined, the disadvantage of plasmonic modes is their high loss, which is caused by the relatively large mode overlap of the optical field with the metal (compared to the reflective case). Owing to the high Joule loss at telecommunication and visible wavelengths, the lasing gain threshold for such cavities can be very large. On the other hand, the negative permittivity of metals not only allows them to support SPP modes, but also enables them to act as efficient mirrors. This leads to the second class of metallo-dielectric cavity modes, which can be viewed as lossy versions of the modes in a perfectly conducting metal cavity. Because the mode volume overlap with the metal is usually smaller than in the plasmonic case, in a cavity supporting this type of mode it is possible to achieve higher resonance quality-factors (Q -factors) and lower lasing gain thresholds, albeit at the expense of reduced mode confinement (compared to plasmonic modes). In general, both types of modes can exist in a metal cavity. Embedding the gain disk mentioned earlier in a gold shield (Figure 1.1c) effectively confines the resonant modes while increasing Joule losses. As discussed, the surface bound plasmonic mode (Figure 1.1e) has both a higher M number and higher losses ($M=6$, $Q=36$) compared to the non-plasmonic mode (Figure 1.1d, $M=3$, $Q=183$). It should be noted that even though the metal shield is the source of Joule loss, the large refractive index of the semiconductor core ($n_{\text{semi}} \approx 3.4$) aggravates the problem and increases both the plasmonic and Fresnel reflection losses. For SPP propagation on a (planar) semiconductor–metal interface, the threshold gain for lossless propagation is proportional to n_{semi}^3 [8]. This means that, even though plasmonic modes with relatively high Q can exist inside metal cavities with low-index cores (for example, silica, for which $n=1.48$), using this approach to create a purely plasmonic, room-temperature semiconductor laser at telecommunication wavelengths becomes challenging, due to the order of magnitude increase in gain threshold. However, plasmonic modes also have an advantage in co-localizing the emitters with the resonant mode volume, thereby leading to a more efficient emission into the lasing mode. This mode of operation is discussed further below, but at this point we focus on novel composite metal-dielectric resonators and the resonant modes that they support.

One possible solution for overcoming the obstacle of metal loss is to reduce the temperature of operation, which will have two coinciding benefits: a reduction of the Joule losses in the metal and an increase in the amount of achievable semiconductor gain. Hill and colleagues [9] have demonstrated cryogenic lasing from gold-coated semiconductor cores with diameters as small as 210 nm. However, in this case the metal is directly deposited on the semiconductor core (with a 10-nm SiN electrical insulation layer between). As a result, owing to the large overlap of the mode with the metal, the estimated room-temperature cavity Q is quite low. The best case is ~ 180 for a silver coating (assuming the best reported value for the permittivity of silver [10]) which corresponds to an overall gain threshold of $\sim 1700 \text{ cm}^{-1}$ and is quite challenging to achieve at room temperature. Even though this device lases when cooled to cryogenic temperatures, it would be challenging to achieve

room-temperature lasing with the same approach and a similar sized cavity, owing to the constraints imposed by the amount of available semiconductor gain and the metal losses. The gain coefficient for optically pumped bulk InGaAsP emitting at $1.55\ \mu\text{m}$ is reported to be $\sim 200\ \text{cm}^{-1}$ [11]. Electrically pumped multiple quantum wells (MQWs), on the other hand, have been reported to have higher material gain coefficients of over $1000\ \text{cm}^{-1}$ [12]. Furthermore, recent results obtained from Fabry–Perot type metallic nanolasers at room temperature indicate that this level of gain is also achievable in bulk InGaAs [13]. However, even if the required gain is achievable at room temperature, efficient operation of the device would still be a challenge because of thermal heating and nonradiative recombination processes (for example, Auger recombination). In particular, to operate a densely packed array of such devices, thermal management would be a major concern, given the requisite intense pumping levels. Consequently, it is extremely important to optimize the resonator design so that the gain threshold is minimized. In this chapter we introduce novel, composite metal-dielectric, three-dimensional resonators, and lasers that are smaller than the wavelength in all three space dimensions (3D), can operate at room temperatures, and can even operate without a threshold [7, 14–18].

1.2

Composite Metallo-Dielectric-Gain Resonators

As indicated in the previous section, the drawback of using metals in optical resonators is their high dissipative loss. In this section, we show that the losses in metal-coated gain waveguides and in 3D laser resonators, can be significantly reduced by introducing a low-index “shield” layer between the gain medium and the metal [7, 14, 17].

Consider a composite gain waveguide (CGW) having a gain medium cylindrical core, a shield layer, and a metallic coating, as shown in Figure 1.2a [14]. For a given CGW cross-section size, the shield layer thickness is then tuned to maximize the confinement of the electric field in the gain medium and reduce the field penetration into the metal. By doing that, we increase the ability of the device to compensate for the dissipated power with power generated in the gain medium. A direct measure of that ability is the threshold gain, that is, the gain required for lossless propagation [8] in the CGW. The field attenuation in the shield layer resembles that of Bragg fibers [19]. The layer adjacent to the core, in particular, is of high importance [20] and has also been used, for example, to reduce losses in infrared hollow metallic waveguides [21].

Subsequently, we use the CGW model for the design of subwavelength 3D resonators. To confine the light in the longitudinal direction, the CGW is terminated from both sides by a low-index “plug” region covered with metal, which forms the closed cylindrical structure shown in Figure 1.2b.

A more practical nanolaser configuration from a fabrication point of view is the open structure with a SiO_2 substrate shown in Figure 1.2c. The inherent radiation

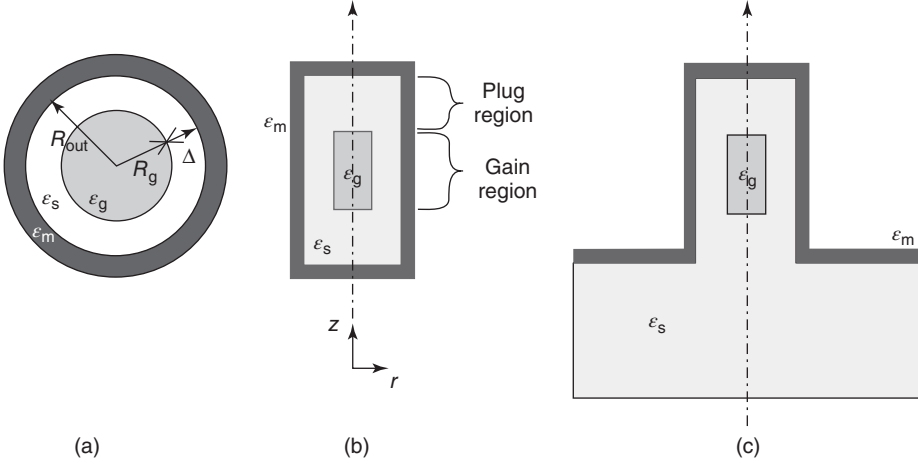


Figure 1.2 (a) Cross section of the metal-coated composite gain waveguide. (b) Cylindrical closed 3D resonator. (c) Cylindrical open 3D resonator. R_g is the radius of the gain core and R_{out} is the overall radius of

the composite gain/dielectric core. Δ is the thickness of the dielectric shield. ϵ_g , ϵ_s , and ϵ_m are the relative permittivities of the gain, shield, and metal layers, respectively. (From [14].)

losses into the substrate provide means for collecting the laser light, in contrast to the closed structure, where extracting light requires modification of the metal coating, such as making an aperture in it. The *threshold gain* for the 3D resonators, defined as the gain required to compensate for the metal losses in the closed structure or to compensate for both the metal and radiation losses in the open structure, is shown in the following sections to be sufficiently low to allow laser action at room temperature.

1.2.1

Composite Gain-Dielectric-Metal Waveguides

We first consider the infinite CGW of Figure 1.2a, with relative permittivities $\epsilon_g = \epsilon'_g + j\epsilon''_g$, ϵ_s , and $\epsilon_m = \epsilon'_m - j\epsilon''_m$ of the gain medium, the shield layer, and the metal, respectively. Assuming a time dependence of $\exp(j\omega t)$, we have $\epsilon''_g > 0$, $\epsilon''_m > 0$. The radius of the gain medium is R_g , the shield layer thickness is $\Delta = R_{out} - R_g$, and the metallic coating layer begins at radius R_{out} . The eigenmodes of the CGW may be derived from the general solution of the longitudinal fields in each layer having the form:

$$U = [AJ_m(k_r r) + BY_m(k_r r)]f(m\varphi) e^{-i\beta z} \quad (1.1)$$

where $U = E_z$ or H_z ; J_m and Y_m are Bessel functions of the first and second kind, respectively; $k_r = \sqrt{k_0^2 \epsilon - \beta^2}$, $k_0 = \omega/c$; ϵ is the relative permittivity of the layer; and $f(m\varphi)$ may be expanded by $\exp(\pm jm\varphi)$, where the integer m is the azimuthal index. The dispersion relation is found using the transfer matrix method [19]. For the

threshold gain ϵ''_g , the propagation constant β is real, and the threshold gain

$$\epsilon''_g = \epsilon''_m \frac{\iint_{\text{Metal}} dA |E|^2}{\iint_{\text{Gain}} dA |E|^2} \quad (1.2)$$

where the integration in the numerator and denominator is over the cross section of the metal and each propagation mode may be found by imposing $\text{Im}\{\beta\} = 0$ in the dispersion relation and then finding the solutions in the plane $(\text{Re}\{\beta\}, \epsilon''_g)$, similarly to [22].

The effect of the shield layer on the TE_{01} mode threshold gain is demonstrated in Figure 1.3, where ϵ''_g is plotted as a function of the shield thickness Δ for a given radius $R_{\text{out}} = 300$ nm (Figure 1.3a) and $R_{\text{out}} = 460$ nm (Figure 1.3b). In the simulations we assume a wavelength of $\lambda = 1550$ nm, $\epsilon'_g = 12.5$ corresponding to an InGaAsP gain medium, $\epsilon'_s = 2.1$ for a SiO_2 shield layer, and $\epsilon_m = -95.9 - j11.0$ for a gold coating [23]. The rapid field decay in the gold layer permits us to assume that the metal extends to infinity, whereas in reality a coating layer of 100 nm would suffice. As the shield thickness increases, a lower percentage of the field penetrates into the metal, reducing the losses. On the other hand, the gain material occupies less of the CGW volume, which means that a higher gain is required to compensate for the dissipation losses in the metal. The trade-off between these two processes results in an optimal point at which the threshold gain is minimal. This typical behavior of low-order modes is seen in Figure 1.3 for the TE_{01} mode. For $R_{\text{out}} = 300$ nm, the improvement of the threshold gain from the $\Delta = 0$ (no shield layer) case is by a factor of 1.7, while for $R_{\text{out}} = 460$ nm, the improvement is by a factor of 6.1.

For larger radii, a lower threshold gain may be achieved, as shown in Figure 1.3 and further emphasized in Figure 1.4, where the minimal threshold gain ϵ''_g is depicted as a function of R_{out} for four low-order modes: TM_{01} , TE_{01} , HE_{11} , and HE_{21} . Having the highest confinement around the gain-medium core, the HE_{11}

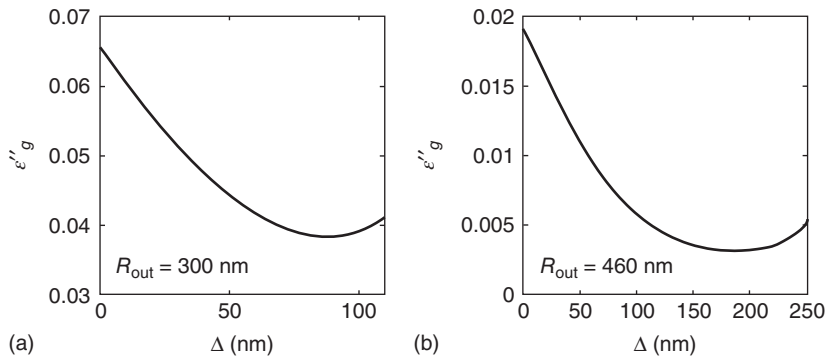


Figure 1.3 Threshold gain ϵ''_g as a function of the shield thickness Δ for the TE_{01} mode. (a) $R_{\text{out}} = 300$ nm. (b) $R_{\text{out}} = 460$ nm. (From [14].)

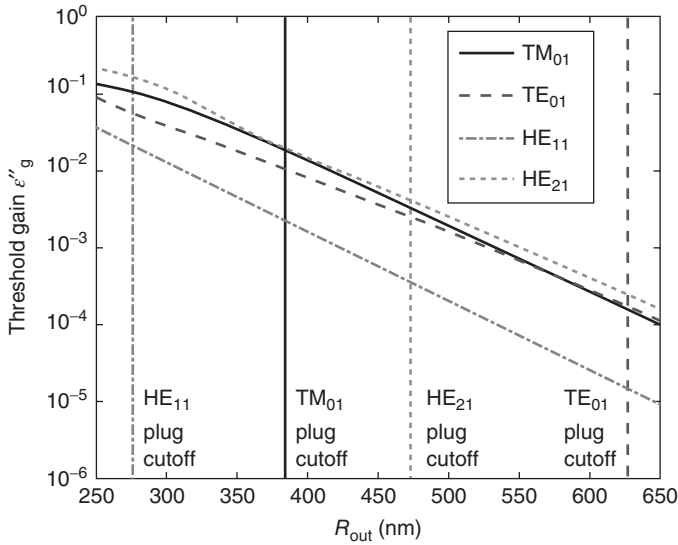


Figure 1.4 Minimum threshold gain as a function of R_{out} . The vertical lines show the cut-off of each mode in the 3D resonator plug region. (From [14].)

mode has the lowest threshold gain among the four modes. Generally, for small radii, the shield layer is less effective, since it quickly drives the mode below the cut-off. For large radii, the threshold gain is low, as the field penetration into the metal is small. The optimal shield layer thickness increases monotonically as a function of R_{out} . For the TE_{01} mode, it ranges between 80 and 330 nm, for a corresponding range of $R_{out} = 250\text{--}650$ nm.

1.2.2

Composite Gain-Dielectric-Metal 3D Resonators

The role of the metal coating, which is important in the infinite CGW model, becomes even more crucial for creating a 3D resonator. As explained above, the CGW facets are terminated by plug regions, which are short metallic waveguides filled with SiO_2 , as seen in Figure 1.2b,c, in an approach similar to that of Hill *et al.* [9]. The plug ensures strong confinement of the field in the gain region, provided that the mode residing in it is below the cut-off, that is, decaying exponentially in the z direction.

For the plug region waveguide, the cut-off is not clearly defined since the modes are significantly different from those of the perfectly conducting cylindrical waveguide [24]. A reasonable definition for the cut-off situation is a waveguide with the radius R_{out} supporting a mode whose β is the closest to the origin on the complex β plane. That cut-off is shown for each one of the modes of Figure 1.4 by the vertical lines, providing a qualitative tool for choosing an operation mode for the entire 3D structure, as the chosen radius needs to be to the left of the

vertical line corresponding to the operation mode. The smaller the device radius compared with the cut-off radius, the stronger the decay in the plug; consequently, the threshold gain is lower. While the HE_{11} mode achieves the lowest threshold gain for a given R_{out} , its cut-off in the plug region is at a small radius; working below this cut-off entails a relatively high threshold gain. It is therefore seen that the TE_{01} mode, which has the highest cut-off of the shown modes, is favorable. The result shows that modes corresponding to a larger R_{out} will have a significantly lower threshold gain. Another advantage of the TE_{01} mode is that in the gain region it couples only to symmetric TE modes in the plug region, whereas $m > 0$ modes are hybrid and may couple to all modes with the same azimuthal index.

Using the CGW model at the optimal point of Figure 1.3b as a starting point, a 3D closed resonator with $R_{\text{out}} = 460$ and a 100 nm thick gold coating was designed for the TE_{012} mode. 3D finite-element method (FEM) simulation results for the squared electric field magnitude $|E|^2$ normalized to its maximum value are shown in Figure 1.5. The overall height of the resonator is 1500 nm, and the overall diameter is 1120 nm, making it smaller than the vacuum wavelength in all three dimensions. The resonance was fine-tuned to a wavelength of 1550 nm by setting the gain cylinder height to be about 480 nm and the shield layer thickness to about 200 nm, which is close to the 190 nm predicted by the CGW model. The threshold gain, however, is in less good agreement with the CGW model; the value for the 3D resonator is $e''_g \approx 0.011$, which corresponds to about 130 cm^{-1} , whereas the CGW model gives about 36 cm^{-1} . This discrepancy is due to the losses occurring in the plug region and the mode deformation at the interfaces between the plug and gain regions, two effects that are not taken into account in the CGW model. It is evident that the longer the resonator, the more accurately the CGW model describes the

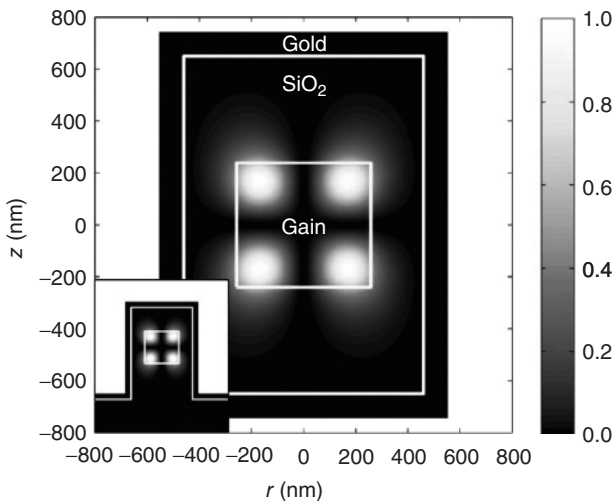


Figure 1.5 Cross section of a closed cylindrical 3D subwavelength laser resonator. The square of the electric field magnitude ($|E|^2$) normalized to its maximal value of the TE_{012} mode is shown. The inset shows a similar open structure.

behavior in the gain region. For instance, a longer resonator with the same radius and designed for the TE_{013} mode has a threshold gain of about 95 cm^{-1} .

If the structure shown in Figure 1.5 is designed with no shield layer in the gain region, but with the same overall radius and height, then the resulting threshold gain is about 420 cm^{-1} . The gain that may be achieved at room temperature by optical pumping of bulk InGaAsP is about 200 cm^{-1} [11]. It is therefore evident that a shield layer that lowers the threshold gain from 420 to 130 cm^{-1} is crucial to enable lasing at room temperature. Slightly modifying the structure for the open configuration, as shown in the inset of Figure 1.5, the field distribution remains nearly unchanged and the threshold gain increases only to about 145 cm^{-1} , owing to the radiation losses. The quality factor of this open resonator without gain is $Q = 1125$, whereas the values for the other 3D structures with a shield layer discussed above are even higher. Finally, we note that for electrical pumping, considerably higher gains may be reached [12] so that the structure, with appropriate changes, is expected to be even further reduced in size. In the following section we use the optimized thickness of a low-index shield layer between the gain medium and the metal coating of a 3D laser resonator for experimental demonstration of nanolasers.

1.3

Experimental Validations of Subwavelength Metallo-Dielectric Lasers for Operation at Room-Temperature

In continuation of the design methodology for 3D subwavelength lasers presented in the previous section, we now present the steps leading to actual implementation and characterization of the devices. The target device is shown in Figure 1.6, in

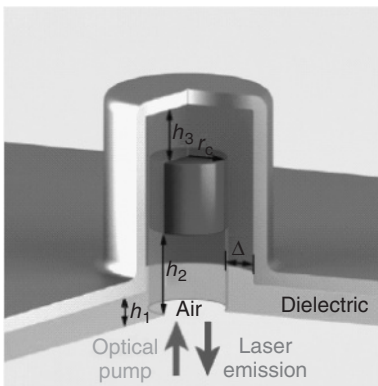


Figure 1.6 Schematic view of a practical realization of the laser cavity, compatible with planar fabrication techniques. The air gap at the bottom of the laser is formed after selective etch removal of the InP

substrate. In the designed cavity the values for h_1 , h_2 , and h_3 are 200, 550, and 250 nm, respectively. (From [7].) (Please find a color version of this figure on the color plates.)

which a gain core is suspended in a bilayer shell of silica and metal. The device is pumped optically through the bottom aperture and the emitted light is also collected from the same aperture.

1.3.1

Fabrication Processes for Subwavelength Metallo-Dielectric Lasers

The metallo-dielectric laser structure was fabricated from an InGaAsP MQW stack grown on InP. Hydrogen silsesquioxane (HSQ) electron-beam resist was patterned into arrays of dots (Figure 1.7a) using a Raith 50 electron-beam writer, and the size of the dots was varied by changing the pattern size and/or the electron-beam dosage. Cylindrical structures were then etched using $\text{CH}_4/\text{H}_2/\text{Ar}$ reactive ion etching (RIE) (Figure 1.7b). Using an optimized and calibrated plasma-enhanced chemical vapor deposition (PECVD) process, the silica shield layer was grown to a thickness of ~ 200 nm (Figure 1.7c). Note that the outline of the embedded gain core is visible through the silica layer. In practice, the poor adhesion of gold to silica caused separation of the dielectric portion of the structure from the metal layer.

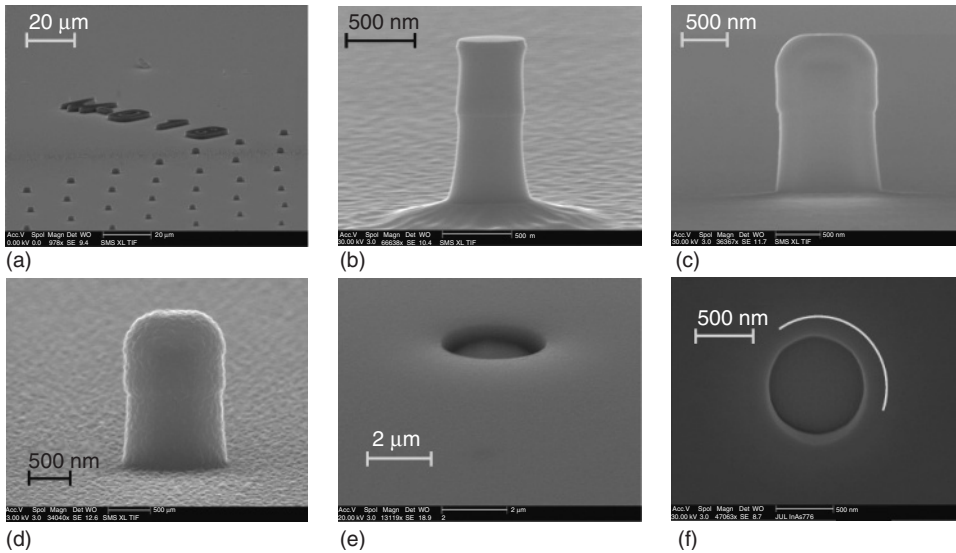


Figure 1.7 Various stages of the fabrication process: (a) Array of electron-beam patterned HSQ resist dots. (b) RIE etched pillar after oxygen plasma and BOE cleaning. The faint bump in the middle indicates the boundary between the InGaAsP and InP layers. (c) Etched pillar after PECVD of silica. The outline of the semiconductor pillar can be seen through the silica layer. (d) Silica covered pillar after undergoing aluminum sputtering (70 nm). (e) Tilted bottom view

of one of the samples after selective InP etch with HCL. The surface is comprised of the PECVD deposited silica. The hole corresponds to the air hole shown in the diagram of Figure 1.6. (f) Contrast enhanced normal bottom view of a cavity. The circular outline around the air hole is due to the dielectric shield layer and agrees well with the target dielectric shield layer thickness of 200 nm. (From [7].)

Fortunately, aluminum exhibits better adhesion properties, and at the wavelength of interest its optical properties are very close to those of gold. (The cavity Q of the resonator with an aluminum coating ($\epsilon_m = -95.9 - j11$) [23] is 1004, which compares with 1030 for gold.) A layer of aluminum with a minimum thickness of 70 nm was sputtered over the silica covered pillars (Figure 1.7d). The sample was then bonded on its upper side to a glass slide using SU-8 resist, and the InP substrate was subsequently removed in a selective HCl etch, leaving an air void under the structure. Figure 1.7e shows the tilted bottom view of an air void, with the lower face of the gain core visible inside. Figure 1.7f shows the normal bottom view (with enhanced contrast levels) of a similar void. The faint outline of the silica shield layer is discernible in this image, verifying the 200 nm thickness of the shield.

1.3.2

Characterization and Testing of Subwavelength Metallo-Dielectric Lasers

For optical pumping we used a 1064 nm wavelength pulsed fiber laser operating at a repetition rate of 300 kHz and a pulse width of 12 ns. The pump beam was delivered to the samples using a $\times 20$ or $\times 50$ long working-distance objective, which also collected the emitted light. To estimate the amount of pump power absorbed by the core, a full three-dimensional finite-element analysis was carried out over a range of core sizes. Using a double 4f imaging system in conjunction with a pump optical filter (Semrock Razor Edge long wavelength pass filter), the samples were imaged onto either an IR InGaAs camera (Indigo Alpha NIR) or a monochromator (Spectral Products DK480) with a resolution of 0.35 nm and equipped with a cooled InGaAs detector in a lock-in detection configuration. Owing to the limitations of the electron-beam writing process, the samples were slightly elliptical. The major and minor diameters of the gain core for the particular sample under test were measured to be 490 and 420 nm, respectively. In Figure 1.8a, the light–light curve corresponding to a laser emitting at 1430 nm is shown and exhibits a slope change that indicates the onset of lasing at an external threshold pump intensity of about 700 W mm^{-2} . The same data set is shown in a log–log plot (Figure 1.8a, inset graph), with the slopes of different regions of operation indicated on the plot. The S-shaped curve clearly shows the transition from photoluminescence (PL) to amplified spontaneous emission (ASE) and finally into the lasing regime. Also shown in Figure 1.8a are the emission patterns of the defocused laser image captured with the IR camera, corresponding to continuous wave (CW) (Figure 1.8a-I) and pulsed (Figure 1.8a-II) pumping situations. The average pump intensity in each case was approximately 8 W mm^{-2} .

Only broad PL emission occurs in the CW case, owing to the low peak intensity. However, when the pump is switched to pulsed mode, lasing is achieved due to the 278-fold increase in peak power. At the same time, the defocused image forms a distinct spatial mode with increased fringe contrast, which is an indication of increased spatial coherence and is further evidence of lasing. The polarization of the emission has a strong linear component, which is attributable to the slight ellipticity

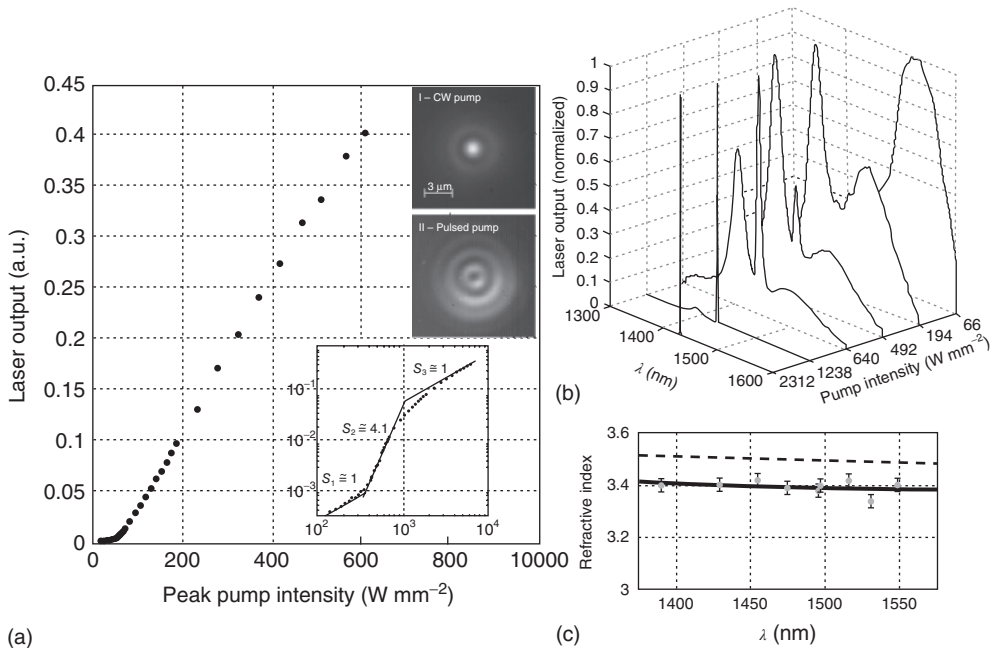


Figure 1.8 (a) Light–light curve for a nanolaser with major and minor core diameters of 490 and 420 nm (dotted curve). The same data set is shown as a log–log plot (dotted inset) together with the slopes for the PL, ASE, and lasing regions. Also shown are the images of the defocused emitted beam cross section (taken at about $10 \mu\text{m}$ away from the nanolaser exit aperture) for (I) CW pumping and (II) pulsed pumping. The appearance of the higher contrast fringes indicates increased coherence due to lasing. (b) Evolution of the emission spectra from PL to lasing. (c) Effective refractive indices (error bar data points) of the pumped MQW

gain medium at lasing wavelengths, back-calculated from lasing spectra obtained from an array of nanolasers. Error bars were calculated assuming $\pm 5 \text{ nm}$ error in measuring the disk diameters from the SEMs. The dashed curve shows the effective refractive index of the unpumped MQW layer, as measured by a Filmetrics interferometric analyzer. The solid curve is offset down from the dashed one by a constant amount (0.102 RIU) that was chosen for best fit to the lasing data. The index reduction is consistent with the estimated free carrier effects. (From [7].)

of the gain core. Figure 1.8b shows the evolution of the emission, from a broad PL spectrum to a pair of competing ASE peaks and finally into a narrow lasing line at 1430 nm. The measured linewidth of this particular laser was 0.9 nm; however, linewidths as small as 0.5 nm were measured for other samples in the same size range.

Another way to verify the soundness and accuracy of the design and fabrication processes is to match the lasing wavelength with the target resonance of the cavity. However, owing to the high pump intensity, the refractive index of the gain core can vary substantially from its quiescent value which can shift the lasing line considerably from its target wavelength. Using the measured results from

an array of lasers with slightly different sizes (which were measured individually using a scanning electron microscope, SEM) and exact three-dimensional finite-element modeling of each of the gain cores, the refractive index of the gain medium under specific pumping conditions was estimated at each lasing point (Figure 1.8c). Assuming a uniform drop in the refractive index over the spectrum of interest and using a least-squares fit of these data points, the estimated drop is ~ 0.102 refractive index units (RIUs) (least-squares fit) less than that obtained from interferometric multilayer measurements of the unpatterned wafers under low illumination intensity (Figure 1.8c, dashed line). We believe that this shift is mainly due to free carrier effects (a combination of band filling, bandgap shrinkage, and free carrier absorption), the net effect of which, at the estimated carrier density (about $1.2 \times 10^{19} \text{ cm}^{-3}$ for a 520 nm diameter core) is a refractive index drop of about 0.1 RIU. Furthermore a slight additional contribution (at most -0.004 RIU) may also be present due to compressive pressure on the gain cores, which is exerted by the thermal shrinkage of the aluminum layer after deposition in the sputtering chamber.

1.4

Electrically Pumped Subwavelength Metallo-Dielectric Lasers

The metallo-dielectric nanolaser described in the previous section is an optically pumped device. An electrically pumped device is more likely to lead to practical applications. In standard semiconductor fabrication technology, electrical contacts are usually implemented by using highly doped semiconductors. Apart from the increased optical losses that would result from the interaction of the optical mode with these highly doped regions, the vertical confinement of the resonator would also be compromised, since the higher index of the semiconductor would adversely affect the operation of the vertical “plugs.” However, in this section we demonstrate that, through a careful design process and judicious selection of device parameters, both of these challenges can be surmounted.

1.4.1

Cavity Design and Modeling of Electrically Pumped Subwavelength Metallo-Dielectric Lasers

The platform for our devices is an InGaAs/InP double heterostructure grown on an InP substrate similar to the structure reported in [9]. The schematic of the laser structure is shown in Figure 1.9a. The intrinsic 300 nm thick (h_{core}) InGaAs bulk layer is the active layer and the upper (470 nm thick) and lower (450 nm thick) InP layers are the cladding layers through which the injected carriers flow into the active layer. Highly doped n-InGaAs on the top and p-InGaAsP in the lower cladding layer form the n- and p-contact layers, respectively. The width of the top and bottom InP cladding layers is intentionally reduced using selective wet etching to form a pedestal structure for enhancing the vertical optical

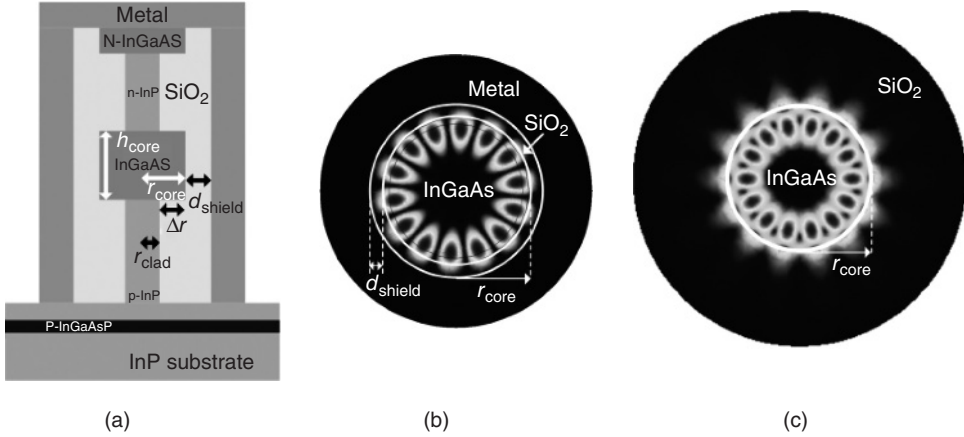


Figure 1.9 A schematic of subwavelength pedestal pillar laser shown in (a) where r_{core} is the radius of InGaAs gain layer, r_{clad} is the radius of InP cladding. Δr is the difference between r_{core} and r_{clad} . d_{shield} is the thickness of SiO_2 shield layer. h_{core} is the height of InGaAs gain medium. (b) The horizontal cross section of the electric field

magnitude when r_{core} is 750 nm, r_{clad} is 690 nm ($\Delta r = 60$ nm), and d_{shield} is 150 nm with silver coating. (c) The horizontal cross section of the electric field magnitude in the same structure with only low-index dielectric (SiO_2) coating. r_{core} in (b,c) are the same value of 750 nm. (From [15].)

confinement. Thin dielectric and metal layers are coated on the pillar structure, thereby forming a metallo-dielectric cavity. As shown in the previous sections, the metallo-dielectric cavity is able to achieve efficient lateral mode confinement at the subwavelength scale due to the high reflectivity of the metal, while reducing the optical ohmic loss by minimizing the mode overlap with the metal by using a thin dielectric shield layer [7, 14]. The dielectric constant of bulk silver at room temperature ($\epsilon_{\text{Ag}} = -120.43 - j3.073$ at $1.55 \mu\text{m}$) was used to simulate the metal coating [10]. We first designed a wavelength scale cavity in which the gain-core radius (r_{core}) is 750 nm ($2r_{\text{core}} \sim \lambda$), the cladding radius (r_{clad}) is 690 nm ($\Delta r = 60$ nm) and the thickness of the SiO_2 shield layer (d_{shield}) is 150 nm. The magnitude of the electric field (horizontal cross section) in the gain medium is shown in Figure 1.9b. A WGM with the azimuthal mode number (M) of 7 is supported and the electric field is strongly confined inside the metal cavity (TE mode). The thin active layer ($h_{\text{core}} = 300$ nm) allows only the lowest order mode in the vertical direction. The modal overlap with the metal coating is minimized by the dielectric shield, as shown in Figure 1.9b. As the dielectric shield layer becomes thinner, the field penetration into the metal coating increases, which results in a higher loss. In contrast, a thick dielectric shield layer could reduce the field penetration into the metal, resulting in a lower gain. Therefore, as discussed earlier, there should be an optimum thickness of the dielectric shield for a given gain-core radius.

For comparison, we numerically modeled the same pedestal structure coated only by a low-index dielectric ($n_{\text{SiO}_2} = 1.45$) and without a metal coating. The

electric field magnitude of the resonant mode of this dielectric cavity is shown in Figure 1.9c. It shows significant modal spreading outside the gain medium, which results in low modal overlap with the gain medium, defined as a confinement factor. In our calculation, the confinement factor in the gain medium of the metallo-dielectric cavity (Figure 1.9b) is 0.39 compared to 0.19 in the purely dielectric cavity case (Figure 1.9c). The Q -factor of the metallo-dielectric cavity is 726, which is a factor of enhancement 5 on the Q -factor of the purely dielectric cavity ($Q = 151$). When the gain-core size is decreased below the wavelength scale, the effective confinement factor is significantly degraded, due to the radiation loss, which is something that has been studied for micro-disk resonators [25, 26]. Figure 1.10a shows the resonant mode of a purely dielectric cavity where $r_{\text{core}} = 350$ nm and $r_{\text{clad}} = 310$ nm ($\Delta r = 40$ nm) with a low-index dielectric (SiO_2) coating. This structure supports a WGM with $M = 3$ that exhibits a significant amount of mode spreading outside the gain medium and a low confinement factor in the gain medium (0.38).

However, by incorporation of the metallo-dielectric cavity (150 nm thick SiO_2 and Ag coating) as shown in Figure 1.10b, the resonant mode is strongly confined inside the subwavelength-scale cavity and the modal overlap with the gain is also significantly enhanced. In our calculation, the confinement factor in the gain medium for the metallo-dielectric cavity is 0.57. In consequence, for such small size resonators this structure produces 22 times increase in the Q -factor of the metallo-dielectric cavity ($Q = 468$), when compared to the Q -factor of the purely dielectric cavity ($Q = 21$). The metallo-dielectric cavity enables further reduction of the gain-core size while keeping efficient mode confinement in the gain medium. We numerically calculated the resonant mode of the metallo-dielectric cavity with $r_{\text{core}} = 220$ nm, $r_{\text{clad}} = 160$ nm ($\Delta r = 60$ nm), and $d_{\text{shield}} = 150$ nm. As shown in Figure 1.10c, for this case, the resonant mode is an axially symmetric mode (TE_{011})

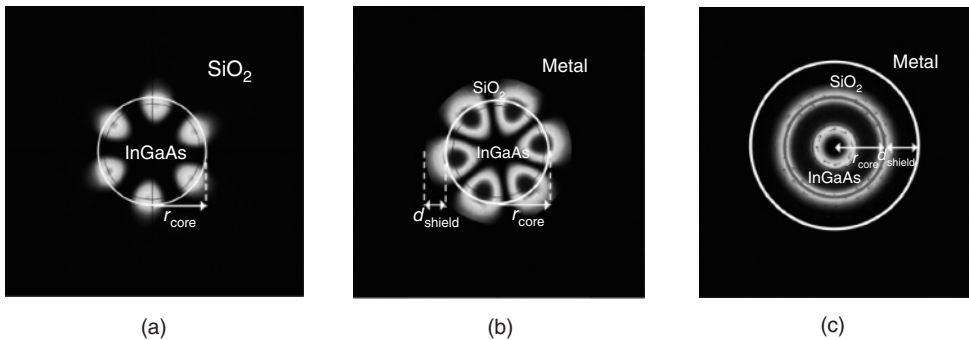


Figure 1.10 The electric field magnitude at the horizontal cross section of the active layer. (a) Pure dielectric cavity with $r_{\text{core}} = 350$ nm, $r_{\text{clad}} = 290$ nm ($\Delta r = 60$ nm), and SiO_2 coating. (b) Metallo-dielectric cavity with $r_{\text{core}} = 350$ nm, $r_{\text{clad}} = 290$ nm ($\Delta r = 60$ nm), $d_{\text{shield}} = 150$ nm, and Ag

coating. The gain structure sizes, r_{core} and r_{clad} , in (a,b) are the same and the resonant mode is WGM with $M = 3$ for both cases. (c) Metallo-dielectric cavity with $r_{\text{core}} = 220$ nm, $r_{\text{clad}} = 160$ nm, $d_{\text{shield}} = 150$ nm, and Ag coating. The resonant mode is axially symmetric TE_{011} mode. (From [15].)

where the electric field circulates around the gain core and is well-confined in the gain medium. The electric field is mostly contained inside the gain medium and has minimal mode overlap with the metal region. The Q -factor of this resonator is calculated to be 707 with a threshold gain of 236 cm^{-1} , which is lower than the bulk gain of InGaAs (400 cm^{-1}) at room temperature, at a wavelength of $1.5 \mu\text{m}$ [27]. The pedestal geometry is adopted in our metallo-dielectric cavity pillar laser structure to enhance the optical confinement in the vertical direction, while maintaining a conduit for carrier flow of both electrons and holes. To analyze the effect of the pedestal in our laser structure quantitatively, we have calculated the Q -factor and the threshold gain by varying r_{clad} .

The calculated Q -factor and threshold gain for a 750 nm core radius with various r_{clad} values is presented in Figure 1.11a. The shield thickness (d_{shield}) and the metal coating were kept constant. When r_{clad} is the same as r_{core} (cylinder type), the Q -factor is 163, and the threshold gain is 1505 cm^{-1} . As r_{clad} is reduced to 600 nm (pedestal type, $\Delta r = 150 \text{ nm}$), the Q -factor is enhanced to 1731, which is about an order of magnitude improvement, and the threshold gain is decreased to 99 cm^{-1} , which represents a 93% reduction. As the pedestal undercut is made deeper (Δr is larger), the threshold gain is flattened and the resonant wavelength is shifted out of the optimal gain spectrum which is undesirable. We have also calculated the Q -factor and threshold gain when $r_{\text{core}} = 220 \text{ nm}$ as the pedestal size is changed, which is shown in Figure 1.11b. The Q -factor is enhanced from 152 (cylinder type, $\Delta r = 0 \text{ nm}$) to 1572 (pedestal type, $\Delta r = 150 \text{ nm}$), which is an order of magnitude improvement. The resonant mode is strongly confined inside the gain layer for the pedestal structure as shown in Figure 1.11d, – where $r_{\text{core}} = 220 \text{ nm}$ and $\Delta r = 120 \text{ nm}$ – and may be compared with the cylinder type structure shown in

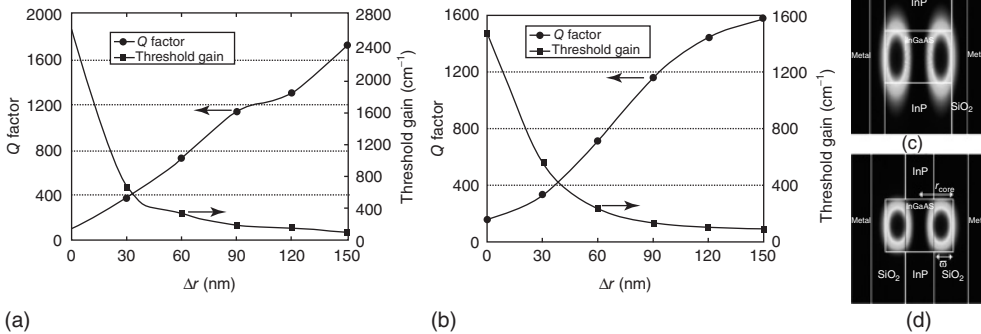


Figure 1.11 Numerical simulation results of the cavity Q -factor and threshold gain for various pedestal sizes. Δr ($= r_{\text{core}} - r_{\text{clad}}$) is pedestal undercut depth. (a) $r_{\text{core}} = 750 \text{ nm}$, $d_{\text{shield}} = 150 \text{ nm}$, and r_{clad} is varied from 750 to 600 nm ($\Delta r = 0 - 150 \text{ nm}$). (b) $r_{\text{core}} = 220 \text{ nm}$, $d_{\text{shield}} = 150 \text{ nm}$, and r_{clad} is varied from 220 to 70 nm ($\Delta r = 0 - 150 \text{ nm}$).

(c) Vertical cross section of the resonant mode field (TE_{011}) magnitude when $r_{\text{core}} = 220 \text{ nm}$, $r_{\text{clad}} = 220 \text{ nm}$ ($\Delta r = 0 \text{ nm}$, cylinder type), and $d_{\text{shield}} = 150 \text{ nm}$. (d) The resonant mode field (TE_{011}) magnitude when $r_{\text{core}} = 220 \text{ nm}$, $r_{\text{clad}} = 100 \text{ nm}$ ($\Delta r = 120 \text{ nm}$, pedestal type), and $d_{\text{shield}} = 150 \text{ nm}$. (From [15].)

Figure 1.11c. The threshold gain is reduced from 1473 to 89 cm^{-1} , which is a 94% reduction. The threshold gain of 89 cm^{-1} is a promising result for the possible room temperature operation of this laser structure. As shown in both cases, the threshold gain is significantly reduced when a minimal pedestal undercut is employed. At $\Delta r = 60\text{ nm}$, the threshold gain for 750 and 220 nm r_{core} values are 338 and 236 cm^{-1} , respectively, and are therefore still lower than our target threshold gain of 400 cm^{-1} [27]. This reduction in the threshold gain has other advantages, since heat dissipation and carrier diffusion in the active layer have been identified as critical issues for most pedestal-type micro-disk lasers [28, 29].

1.4.2

Fabrication of Electrically Pumped Subwavelength Metallo-Dielectric Lasers

Wavelength scale (750 nm radius) and subwavelength scale (355 nm radius) circular masks were patterned on an InGaAs/InP heterostructure wafer by means of electron-beam lithography (EBL), using spin-coated HSQ resist. Subsequent dry etching was performed using $\text{CH}_4/\text{H}_2/\text{Ar}$ gas chemistry to form subwavelength-scale pillar structures (as in the SEM image shown in Figure 1.12a). The selective etching of the cladding InP layers was performed using $\text{HCl}:\text{H}_3\text{PO}_4$ (1:3) wet etching and the result is shown in Figure 1.12b. 160 nm of InP was etched away on both sides through the wet etching process while the gain layer was preserved. A 150 nm thick layer of SiO_2 was conformally deposited on the pedestal pillar surface by means of a PECVD process (Figure 1.12c), which provides the low-index shield layer required to minimize the mode-metal overlap of the modal field with the metal and also passivates the InGaAs surface.

The SiO_2 layer on top of the subwavelength pillar structure was removed through the photoresist planarization process and SiO_2 dry etching, in order to access the n-side contact layer (n-InGaAs). Metal contacts (Ti/Pd/Au) were formed on the top

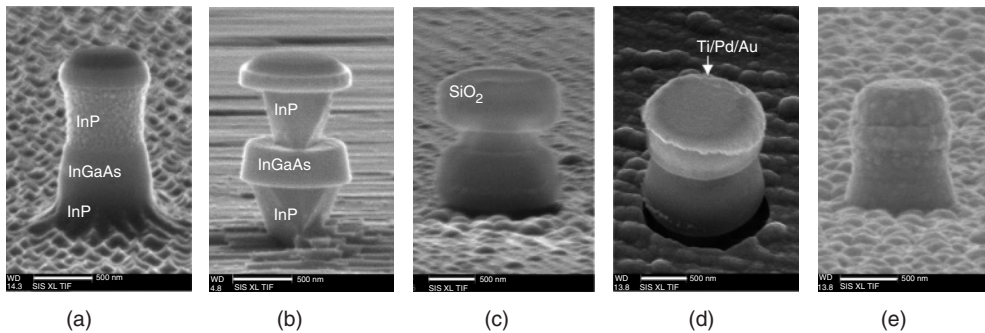


Figure 1.12 SEM images of subwavelength pillar laser structure during fabrication procedure. (a) Subwavelength pillar ($r_{\text{core}} = 395\text{ nm}$) structure after dry etching. (b) Pedestal pillar is formed by selective InP wet etching. (c) A thin SiO_2 layer

(140 nm) is deposited on the pillar structure by PECVD. (d) N-contact metal (Ti/Pd/Au) layer deposited on the top of subwavelength pillar. (e) Silver is deposited on whole pillar structure. The scale bar in each image represents 500 nm . (From [15].)

of the pillar structure by electron-beam evaporation and liftoff (Figure 1.12d). After n-contact formation, a 200 nm thick silver layer was deposited so as to completely cover the pillar structures including the top and side wall of the pillar, and the n-type contact pad (Figure 1.12e). A 20 nm chromium (Cr) layer was deposited prior to the silver deposition for better adhesion. Since the high optical loss of Cr could degrade the Q -factor of the cavity and therefore increase the threshold gain, the unintentionally deposited Cr on the side wall of the pillar structure was subsequently removed by Cr wet etching while protecting the adhesion layer on the substrate by masking with photoresist. The p-contact was processed separately using photolithographic patterning and wet etching of the SiO_2 and InP layers, in order to access the underlying highly doped InGaAsP layer. The sample was then annealed to 400 °C for 60 s to reduce the contact resistance. Finally, the sample was mounted on the device package (TO 8) and wire-bonded.

1.4.3

Measurements and Discussion of Electrically Pumped Subwavelength Metallo-Dielectric Lasers

The devices were forward biased and the CW emission from the device was collected through a $\times 20$ objective lens, and then imaged using a CCD camera. The spectral characteristics were analyzed by a monochromator with a maximum spectral resolution of 0.35 nm (with a 100 μm slit opening). The lasing characteristics of electrically pumped pedestal pillar lasers with two different gain-core radii (750 and 355 nm) were measured and analyzed. Figure 1.13a shows a SEM image of the pedestal pillar, in which $r_{\text{core}} = 750$ nm, $r_{\text{clad}} = 710$ nm, and the pillar height is 1.3 μm . The shield layer thickness (d_{shield}) was 140 nm and silver was coated to form a metal cavity. In the numerical simulation, the Q -factor was estimated to be 458 and the threshold gain was 534 cm^{-1} at the resonant wavelength of 1.50 μm . The lasing characteristics of this device at 77 K are shown in Figure 1.13b. Electroluminescence (EL) around 1.55 μm was observed when the injected current was higher than 20 μA . As the injected current increased, the emission spectrum showed spectral narrowing and the lasing peak appeared at 1.49 μm which is very close to the calculated resonant wavelength of 1.50 μm . The light output–injection current (L – I) curve (Figure 1.13c) shows a kink around the threshold current (50 μA) which is also an indication of the onset of lasing. The linewidth narrowed to 0.9 nm at an injection current level of 300 μA . We also investigated the temperature dependence of the lasing characteristics of this device. A local heater inside the cryostat kept the target temperature constant during the measurement. Lasing behavior was observed at 100, 120, and 140 K at a constant pumping current. The spectral evolution and L – I curve at 140 K are shown in Figure 1.13e. The lasing wavelength remained in the vicinity of 1.49 μm and the linewidth was also less than 1 nm at 140 K (Figure 1.13d). However, the threshold current increased to 240 μA (inset in Figure 1.13e) which is five times higher than the threshold current at 77 K. At 160 K, spectral narrowing was still observed at a wavelength of 1.49 μm , but the

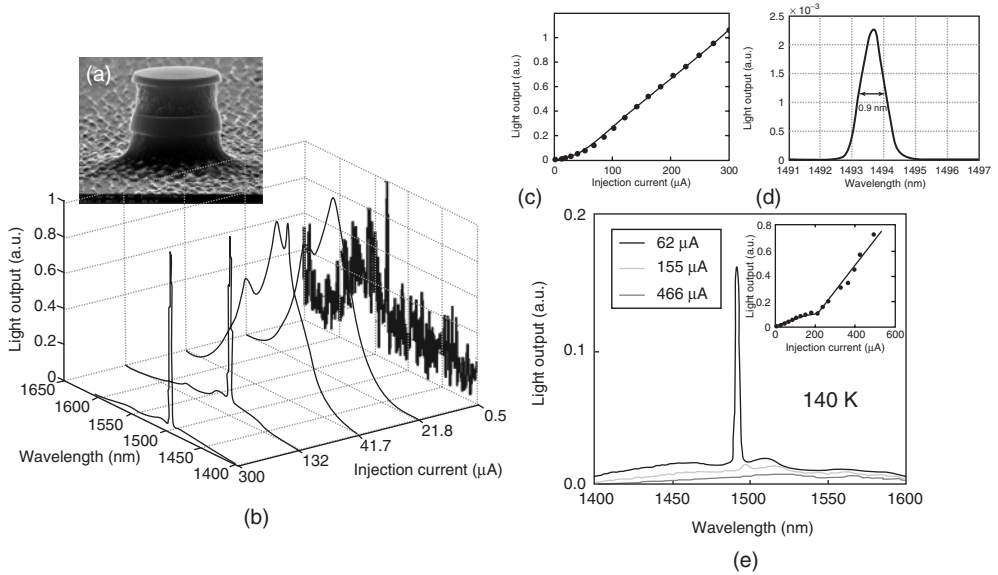


Figure 1.13 Lasing characteristics of 750 nm r_{core} pedestal pillar laser device. (a) An SEM image of the 750 nm r_{core} pedestal pillar structure. (b) Spectral evolution graphs with increasing injection current. (c) $L-I$ curve of this device. (d) Linewidth measurement by a monochromator with 0.35 nm resolution. (e) Lasing spectrum measured at 140 K. The inset shows $L-I$ curve at 140 K. (From [15].)

device failed to reach lasing condition, primarily due to the heat generation inside the cavity and the higher optical losses in the metal cavity.

The lasing characteristics of 355 nm core radius subwavelength pillar laser were also investigated as shown in Figure 1.14. An SEM image of the pedestal pillar structure is shown in Figure 1.14a. The pillar structure had $r_{\text{core}} = 355$ nm, $r_{\text{clad}} = 310$ nm, $d_{\text{shield}} = 140$ nm, together with a 1.36 μm pillar height and silver coating. As discussed in the numerical simulation, this cavity structure supports the WGM with $M = 3$. From the simulation, the Q -factor was estimated to be 352 and the threshold gain was 692 cm $^{-1}$ at the resonant wavelength of 1.38 μm. As shown in Figure 1.14b, spectral narrowing was observed as the injection current was increased and the lasing peak occurred at a wavelength of 1.41 μm. The threshold current was estimated to be around 540 μA which is 10 times higher than for the 750 nm r_{core} device due to the lower material gain at shorter wavelengths and the higher threshold gain value required. The resonant wavelength estimated using the simulation (1.38 μm) matches the measured results quite well. Higher resolution analysis of the lasing peak spectrum showed that the lasing peak at 1.41 μm is in fact a dual peak with 1.5 nm splitting (Figure 1.14d), which indicates the imperfect circular symmetry of the pillar structure because of inaccuracy in fabrication. When the temperature was increased, CW lasing operation was observed up to 100 K. As shown in Figure 1.14e, the onset of the lasing peak was clearly observed and the linewidth was about 6 nm at 100 K. At 120 K, the output

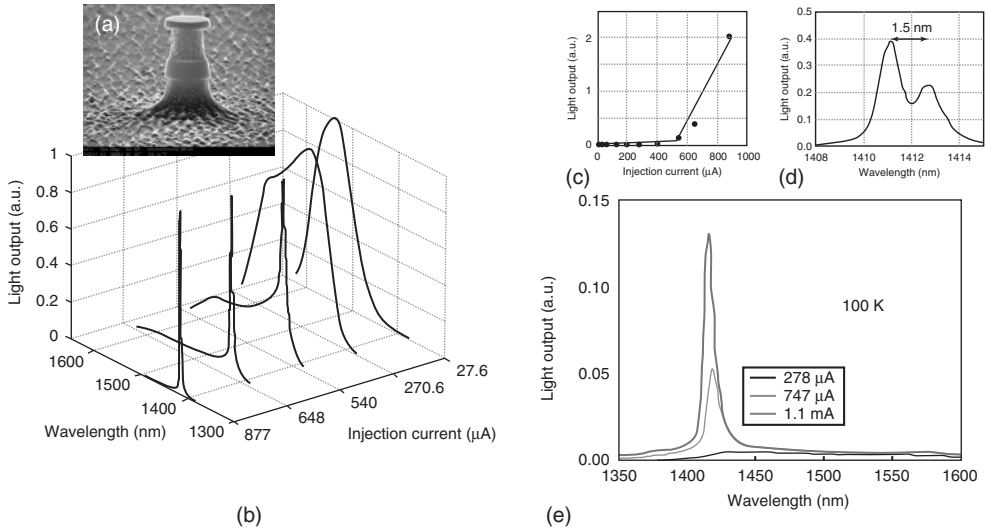


Figure 1.14 Lasing characteristics of 355 nm r_{core} pedestal pillar laser device. (a) An SEM image of 355 nm r_{core} pedestal pillar structure. (b) Spectral evolution graphs with increasing the injection current. (c) $L-I$ curve of this device. (d) Linewidth measurement by a monochromator. (e) Lasing spectrum with difference injection currents measured at 100 K. (From [15].)

spectrum showed clear spectral narrowing with 8 nm linewidth, but failed to reach lasing, which could be due to the heating effect of the high driving current. It is to be expected that pulsed operation would reduce the impact of heating, enabling the device to operate at even higher temperatures. Based on the above numerical simulation, a smaller size ($r_{\text{core}} = 220$ nm) device should be able to lase with a low threshold gain ($< 100 \text{ cm}^{-1}$). However, the fabrication difficulties, such as forming pedestal structures on a 200 nm wide InP cladding layer with the wet etching process, still pose a challenge and the thermal management issue becomes even more critical with subwavelength-scale pillar widths. We are currently working on resolving these issues by optimizing our fabrication processes and developing a low resistance contact design that could reduce the electrical power dissipation and self-heating in the device. Incorporation of quantum well or quantum dot gain structures in our laser devices could also allow for the building of highly efficient subwavelength-scale lasers [7, 30].

1.5 Thresholdless Nanoscale Coaxial Lasers

The devices described in previous sections, although smaller in all three dimensions than the free-space emitted wavelength, remain limited in a fundamental way: the lasing modes are essentially those of a hollow cylindrical metallic waveguide, and are subject to cut-off. Although, as observed in Section 1.2, the exact cut-off

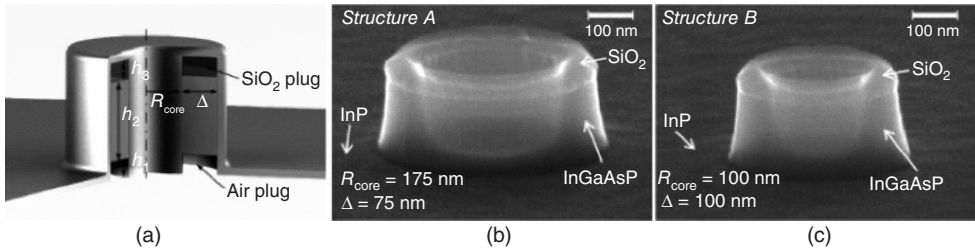


Figure 1.15 Nanoscale coaxial laser cavity. (a) Schematic of a coaxial laser cavity. (b,c) SEM images of the constituent rings in *Structure A* and *Structure B*, respectively. The side view of the rings comprising the

coaxial structures is seen. The rings consist of SiO_2 on top, and quantum wells gain region underneath. (From [18].) (Please find a color version of this figure on the color plates.)

frequencies of the cylindrical structures discussed here differ somewhat from those of a cylinder with perfectly conducting walls, it is still the case that when the structure diameter is significantly smaller than the operating wavelength, modes such as those shown in Figure 1.5 cannot be sustained. One alternative design that could, in principle, permit size reduction beyond this limit is based on a coaxial waveguide geometry (Figure 1.15), which supports a TEM-like mode with no cut-off [18].

Coaxial nanolasers are also of theoretical interest because it is possible to design a cavity with the mode structure so sparse that only one mode falls within the gain bandwidth of the semiconductor core. A laser of this type exhibits a high spontaneous emission factor β (the ratio of spontaneous emission into the lasing mode to all spontaneous emission) that approaches unity and a pronounced Purcell effect [31] (enhancement or inhibition of spontaneous emission into the lasing mode compared to emission into free space, characterized by the Purcell factor). As a consequence, the characteristic kink in the log-scale light–light curve of the laser becomes smoothed out and less recognizable. Thresholdless laser behavior would imply a smooth curve throughout the pumping region, until saturation is reached. The theory of such lasers, particularly the modeling of subthreshold behavior and the definition of the lasing threshold, is an area of active research, It is also worth noting that, other things being equal, a large β value and strong Purcell enhancement tend to reduce the pump power required to obtain coherent radiation.

The cavity quantum electrodynamic (QED) effects caused by the interaction of matter and the electromagnetic field in subwavelength structures have been the subject of intense research in recent years [32]. The generation of coherent radiation in nanostructures has attracted considerable interest, both because of the QED effects that emerge in small volumes, and the potential of these devices for future applications, ranging from on-chip optical communication to ultrahigh resolution and high throughput imaging/sensing/spectroscopy [33, 34]. Current research efforts are directed at developing the “ultimate nanolaser”: a scalable, low threshold, efficient source of radiation that operates at room-temperature, and occupies a small volume on a chip [35]. Coaxial nanostructures help to reach

these goals, demonstrating the smallest volume laser device that operates at room temperature in CW mode and at telecom wavelengths. More importantly, for the first time, we have demonstrated thresholdless lasing with a broadband gain medium. Besides their application in the realization of deep subwavelength lasers, nanoscale coaxial resonators are the first step toward unveiling the potential of QED objects and meta-materials in which atom–field interactions generate new functionalities [36, 37].

1.5.1

Design and Fabrication of Thresholdless Nanoscale Coaxial Lasers

The miniaturization of laser resonators using dielectric or metallic material structures, faces two challenges: (i) the (eigen-) mode scalability, implying the existence of a self-sustained electromagnetic field, regardless of the cavity size and (ii) the unbalanced rate of decrease in the optical gain versus cavity loss, which results in a large and/or unattainable lasing threshold, as the volume of the resonator is reduced [25]. In this section, we describe and demonstrate a new approach to nanocavity design that resolves both challenges: firstly, subwavelength size nanocavities with modes far smaller than the free space operating wavelength are realized by designing a plasmonic coaxial resonator that supports the cut-off-free transverse electromagnetic (TEM) mode. Secondly, the high lasing threshold for small resonators is reduced by utilizing cavity QED effects, causing high levels of coupling of spontaneous emission into the lasing mode [38, 39]

The coaxial laser cavity is portrayed in Figure 1.15a. At the heart of the cavity lies a coaxial waveguide that supports plasmonic modes and is composed of a metallic rod enclosed by a metal-coated semiconductor ring [40, 41]. The impedance mismatch between a free-standing coaxial waveguide mode and free-space creates a resonator. However, our design uses additional metal coverage on top of the device, thin, low-index dielectric plugs of silicon dioxide at the top end, and air at the bottom end of the coaxial waveguide in order to improve the modal confinement. The role of the top SiO₂ plug is to prevent the formation of undesirable plasmonic modes at the top interface between the metal and the gain medium. The lower air plug enables coupling of the pump light into the cavity and also the coupling out of the light generated in the coaxial resonator. The metal in the sidewalls of the coaxial cavity is placed in direct contact with the semiconductor to ensure the support of plasmonic modes, providing a large overlap between the modes of the resonator and the emitters distributed in the volume of the gain medium. In addition, the metallic coating serves as a heat sink that facilitates room temperature and CW operation.

To reduce the lasing threshold, the coaxial structures are designed to maximize the benefits from the modification of the spontaneous emission due to the cavity QED effects [38, 39]. Because of their small size, the modal content of the nanoscale coaxial cavities is sparse, which is a key requirement for obtaining coupling of a high level of spontaneous emission into the lasing mode of the resonator. The modal content can be further modified by tailoring the geometry, that is,

the radius of the core, the width of the ring, and the height of the gain and low-index plugs. Note that the number of modes supported by the resonator that can participate in the lasing process is ultimately limited to those that occur at frequencies that coincide with the gain bandwidth of the semiconductor gain material. In this work we have used a semiconductor gain medium composed of six quantum wells of $\text{In}_{x=0.56}\text{Ga}_{1-x}\text{As}_{y=0.938}\text{P}_{1-y}$ (10 nm thick) between barrier layers of $\text{In}_{x=0.734}\text{Ga}_{1-x}\text{As}_{y=0.57}\text{P}_{1-y}$ (20 nm thick), resulting in a gain bandwidth that spans frequencies corresponding to wavelengths in vacuum that range from 1.26 to 1.59 μm at room temperature, and from 1.27 to 1.53 μm at 4.5 K [42].

We consider two different versions of the geometry shown in Figure 1.15a, the first, referred to as *Structure A*, has an inner core radius of $R_{\text{core}} = 175$ nm, gain medium ring with a thickness of $\Delta = 75$ nm, lower plug height of $h_1 = 20$ nm, and quantum wells height of 200 nm covered by a 10 nm overlayer of InP resulting in a total gain medium height of $h_2 = 210$ nm, and upper plug height of $h_3 = 30$ nm. The second, *Structure B* is smaller in diameter, having $R_{\text{core}} = 100$ nm, and $\Delta = 100$ nm. The heights of the plugs and the gain medium are identical to those of *Structure A*. Figure 1.15b,c show the SEM images of the constituent rings in *Structure A* and *Structure B*, respectively. The two structures are fabricated using standard nanofabrication techniques.

Figure 1.16 shows the modal content of the two structures at 4.5 K, modeled using the 3D FEM eigenfrequency solver in the RF package of COMSOL Multiphysics. Figure 1.16a shows that for *Structure A* the fundamental TEM-like mode and the two degenerate HE_{11} modes are supported by the resonator and fall within the gain bandwidth of the gain material. This simulation was also repeated for *Structure A* with room temperature material parameters, showing that the two degenerate HE_{11} modes are redshifted to 1400 nm, and exhibit a reduced resonance quality factor of $Q \approx 35$, compared to $Q \approx 47$ at 4.5 K. The TEM-like mode is red shifted to 1520 nm with $Q \approx 53$, compared to $Q \approx 120$ at 4.5 K.

Structure B, shown in Figure 1.16b, supports only the fundamental TEM-like mode at a temperature of 4.5 K. The quality factor $Q \approx 265$ for this mode is higher than that of *Structure A*. In general, the metal coating and the small aperture of the nanoscale coaxial cavity inhibit the gain emitters from coupling into the continuum of free-space radiation modes [43]. Hence, the single-mode cavity of *Structure B* exhibits a very high spontaneous emission coupling factor ($\beta \approx 0.99$), approaching the condition for an ideal thresholdless laser [38, 39]. The spontaneous emission factor is calculated by placing randomly oriented and randomly positioned dipoles in the active area of the cavity, and then computing their emitted power at different wavelengths. The β -factor is given by the emitted power that spectrally coincides with the lasing mode, divided by the total emitted power [44].

1.5.2

Characterization and Discussion of Thresholdless Nanoscale Coaxial Lasers

Characterization of the nanoscale coaxial lasers was performed under optical pumping with a $\lambda = 1064$ nm laser pump beam, in both CW and pulsed regimes.

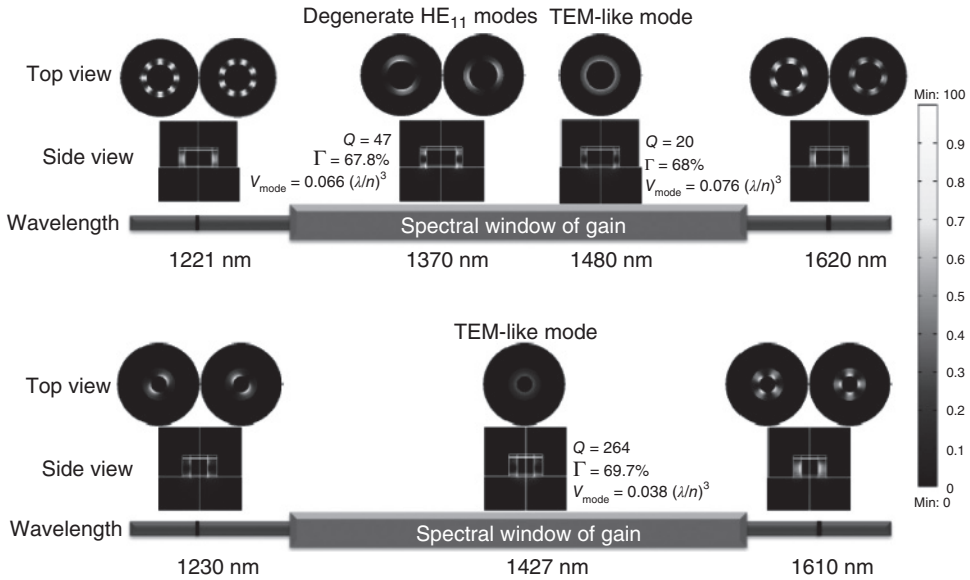


Figure 1.16 Electromagnetic simulation of nanoscale coaxial cavities. (a) The modal spectrum of the cavity of *Structure A* at a temperature of 4.5 K. This cavity supports a pair of HE_{11} degenerate modes and the fundamental TEM-like mode, within the gain bandwidth. (b) The modal spectrum of the cavity of *Structure B*. This cavity only supports the fundamental TEM-like mode

within the gain bandwidth of the quantum wells. In the figures, Q is the quality factor of the mode, Γ is the energy confinement factor of the semiconductor region [21] and V_{mode} is the effective modal volume [22]. The color bar shows normalized $|E|^2$. Nominal permittivity values are used in this simulation. (From [18].)

Excitation of the cavity modes is confirmed by measurements of the far-field emission from the devices.

Figure 1.17 shows the emission characteristics of the nanoscale coaxial laser of *Structure A* operating at 4.5 K (light–light curve in frame (a)), spectral evolution in frame (b), linewidth in frame (c)), and at room temperature (light–light curve in frame (d)), spectral evolution in frame (e), and linewidth in frame (f)). The light–light curves of Figure 1.17a,d show standard laser action behavior, where spontaneous emission dominates at lower pump powers (referred to as the *photoluminescence region*), and stimulated emission is dominant at higher pump powers (referred to as the *lasing region*). The PL and lasing regions are connected through a pronounced transition region, referred to as the *amplified spontaneous emission region*. The evolution of the spectrum shown in Figure 1.17b,e also confirms the three regimes of operation: PL, ASE, and lasing. The spectral profiles at low pump powers reflect the modification of the spontaneous emission spectrum by the cavity resonances depicted in Figure 1.16a. The linewidth of the lasers shown in Figure 1.17c,f narrows with the inverse of the output power at lower pump levels (the solid trend line), which is in agreement with the well-known Schawlow–Townes formula

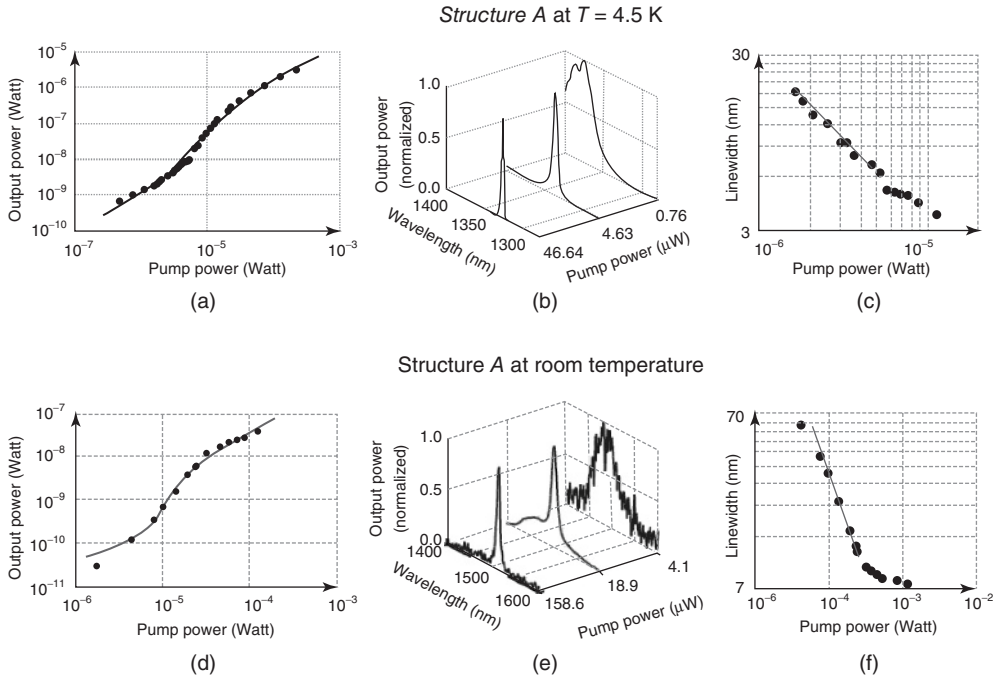


Figure 1.17 Optical characterization of nanoscale coaxial cavities, light–light curve, linewidth versus pump power, and spectral evolution diagram for lasers with threshold. Lasing in *Structure A*. (a) Light–light curve, (b) spectral evolution and (c) linewidth evolution at 4.5 K, (d) light–light curve, (e)

spectral evolution, and (f) linewidth at room temperature. The pump power is calculated as the fraction of the power incident on the laser aperture. The solid curves in (a,d) are the best fit of the rate-equation model. The resolution of the monochromator was set to 3.3 nm. (From [18].)

for lasers operating below threshold [45]. Around threshold, the rapid increase in the gain–index coupling in semiconductor lasers slows down the narrowing of the linewidth, until carrier pinning resumes the modified Schawlow–Townes inverse power narrowing rate [46, 47]. In practice, only a few semiconductor lasers are shown to have above-threshold linewidth behavior that follows the modified Schawlow–Townes formula. In most of the lasers reported in the literature, the linewidth behavior is distinctly different from the inverse power narrowing rate. The mechanisms affecting the above-threshold linewidth, especially for lasers with high spontaneous emission coupling to the lasing mode, still constitute an important area of research [48–50].

A rate-equation model was adopted to study the dynamics of the photon-carriers interaction in the laser cavities. The light–light curves obtained from the rate-equation model for the laser of *Structure A* are shown as solid lines in Figure 1.17a,d. For the laser operating at 4.5 K, by fitting the rate-equation model to the experimental data, we found that almost 20% of the spontaneous emission is coupled into the lasing mode, which is assumed to be the mode with the

highest quality factor (TEM-like mode). This assumption is validated by examining the far-field radiation pattern and the polarization state of the output beam. At room temperature, the surface and Auger nonradiative recombination processes dominate. As the carriers are lost through nonradiative channels, the ASE kink of the laser becomes more pronounced, and, as expected, the laser threshold shifts to higher pump powers levels.

Next, we examine the emission characteristics of *Structure B*. According to the electromagnetic analysis (Figure 1.16b), this structure is expected to operate as a thresholdless laser, since only one nondegenerate mode resides within the emission bandwidth of the gain medium. The emission characteristics of *Structure B* at 4.5 K are shown in Figure 1.18. The light–light curve of Figure 1.18a, which follows a straight line with no pronounced kink, agrees with the thresholdless lasing hypothesis. The thresholdless behavior is further manifested in the spectral evolution, seen in Figure 1.18b, where a single narrow, Lorentzian-like emission spectrum is obtained over the entire five-orders-of-magnitude range of pump power. This range spans from the first signal detected above the detection system noise floor at 720 pW pump power, to the highest pump power level of more than 100 μ W. Since the homogeneously broadened linewidth of the gain medium is larger than the linewidth of the observed emission, the emission profile is attributed to the cavity mode. The measured linewidth at low pump power ($\Delta\lambda_{\text{FWHM}} \approx 5$ nm) which agrees with the transparency cavity Q -factor value of the TEM-like mode, as well as the radiation pattern, confirms the electromagnetic simulation given in Figure 1.16b. The evidence that the device indeed reaches lasing is further supported by the linewidth behavior. At low pump levels, the linewidth depicted in Figure 1.18c is almost constant, and does not narrow with output power, implying that the linewidth shows no subthreshold behavior [39, 47]. The lack of variation of linewidth with pump power is most probably the result of the increasing gain-index coupling, which is well-known as around-threshold behavior in semiconductor lasers [46, 47]. Another indication, and a more decisive proof, that *Structure B* does not exhibit subthreshold behavior is that the linewidth narrowing above the 100 nW pump power level does not follow the inverse power narrowing rate that is clearly identified in *Structure A*. This narrowing corresponds to the carrier-pinning effect, as further corroborated by the results of the rate-equation model for the carrier density. To the best of our knowledge, this linewidth behavior, though predicted in theory [48–50], has never been reported in any laser, and is unique to our thresholdless laser. The light–light curve obtained from the rate-equation model for the laser of *Structure B* at 4.5 K is shown by the solid line in Figure 1.18a. The best fit of our rate-equation model to the experimental data is achieved if 95% of the spontaneous emission is coupled to the lasing mode ($\beta = 0.95$). The deviation from the $\beta = 0.99$ value predicted by the electromagnetic simulation can be attributed to other nonradiative recombination processes that have not been considered in the rate-equation model, and to the spectral shift of the mode at higher pump levels that causes variations in the available gain for the mode. In summary, all the experimental observations, including output spectrum and beam profile, electromagnetic simulations, rate-equation model, and comparison with

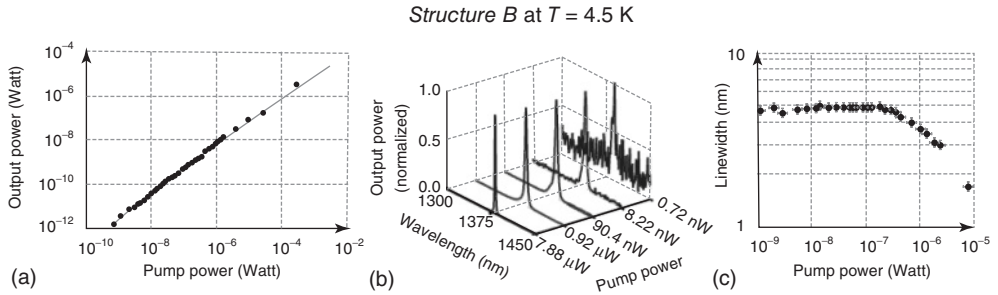


Figure 1.18 Optical characterization of nanoscale coaxial cavities, light–light curve, linewidth versus pump power, and spectral evolution diagram for thresholdless lasers. Thresholdless lasing in *Structure B*. (a) Light–light curve, (b) spectral evolution, and (c) linewidth evolution at 4.5 K.

The pump power is calculated as the fraction of the power incident on the laser aperture. The solid curve in (a) is the best fit of the rate-equation model. The resolution of the monochromator was set to 1.6 nm. (From [18].)

the behavior of non-thresholdless lasers, suggest thresholdless lasing as the only plausible hypothesis that satisfactorily explains all aspects of the emission from the light emitting device, based on our results for *Structure B* at 4.5 K.

The thresholdless lasing that we have demonstrated in nanoscale coaxial cavities clearly differs from the situation in the state-of-the-art, high quality factor, photonic bandgap structures [51]. In the latter, near-thresholdless lasing is achieved in a quantum dot gain medium system with spectrally narrow band emission, and relies extensively on tuning of the cavity mode to the center of the quantum dot emission spectrum [51]. In the former, thresholdless lasing in a broadband gain medium is achieved with a low quality factor, single-mode metal cavity. Smaller size, a straightforward fabrication procedure, and better thermal properties are just a few of the advantages of nanoscale coaxial cavities for the realization of thresholdless lasing.

1.6 Summary, Discussions, and Conclusions

We have introduced and analyzed a new type of composite metallo-dielectric resonator that is confined in all three dimensions [7, 14–18]. We have investigated the effect of a low-index dielectric shield layer between the gain medium and the metal coating of a gain waveguide and a 3D laser resonator.

We have shown that the shield layer in the gain waveguide has an optimal thickness such that the threshold gain required to compensate for losses is minimal. The gain-waveguide results were used to design a novel 3D resonator that is smaller than the vacuum wavelength of the emitted light in all three dimensions, and has a sufficiently low threshold gain to allow lasing at room temperature. Using this design, we have demonstrated room-temperature lasing from subwavelength

metallo-dielectric resonators. In addition to reducing the size below the emission wavelength in all three dimensions, the metal layer isolates the cavity from its outer environment.

The subwavelength nature of these emitters may lead to practical applications such as dense optical interconnects and laser arrays for optical trapping and manipulation of particles, both of which are currently limited by the larger size and lateral coupling effects in vertical-cavity surface-emitting laser (VCSEL) arrays. Also, the small size of the cavity may enable the implementation of high-speed directly modulated lasers through spontaneous emission enhancement by means of the Purcell effect.

We have also demonstrated a new design and fabrication of wavelength and subwavelength scale electrically driven lasers using metallo-dielectric cavities. In the design, the metal cavity, combined with a thin low-index dielectric layer, enabled a significant enhancement in modal confinement for both wavelength and subwavelength-scale cavities. Using a pedestal geometry improved the vertical mode confinement and showed a significant reduction in the threshold gain with increasing undercut in the pedestal cladding. Lowering the threshold gain below the target 400 cm^{-1} requires a minimal undercut ($< 60 \text{ nm}$) in the pedestal for 750 and 350 nm core radius lasers. This approach also provides an advantage for efficient heat transfer and carrier diffusion in the active region. Experimentally, we have presented the fabrication process for our designed structure, which is based on an InGaAs/InP double heterostructure. Laser devices were fabricated for 750 and 355 nm gain-core radii. We observed clear lasing operation at 77 K for both laser devices, with low threshold current values of 50 and $540 \mu\text{A}$, respectively. For the $r_{\text{core}} = 750 \text{ nm}$ laser device, CW lasing operation at $1.49 \mu\text{m}$ was observed up to 140 K. The $r_{\text{core}} = 355 \text{ nm}$ laser device showed CW lasing operation up to 100 K. Numerical studies suggest that even smaller laser structures (core radius = 220 nm) could exhibit low threshold gain, making room temperature operation feasible.

Finally, with nanoscale coaxial resonant structures, we have successfully demonstrated room temperature, CW lasing and low-temperature, thresholdless lasing in a spectrally broadband semiconductor gain medium. Owing to the fundamental TEM-like mode with no cut-off, these cavities show ultrasmall mode confinement, offer a large mode-emitter overlap that results in optimal utilization of the pump power, and provide multifold scalability. Further developments toward electrical pumping of thresholdless nanoscale coaxial lasers that could operate at room temperature are in progress. The implications of our work are threefold. Firstly, the demonstrated nanoscale coaxial lasers have a great potential for future nanophotonic circuits on a chip. Secondly, thresholdless operation and scalability provide the first systematic approach toward the realization of QED objects and functionalities, specifically the realization of quantum meta-materials. Finally, this new family of resonators paves the way to in-depth study of the unexplored physics of emitter-field interaction.

It should be noted, however, that as the size of metallo-dielectric coherent sources is made smaller and smaller, the metallic losses become extremely high – due to

the fact that a large portion of the mode overlaps with the metal in cases of extreme confinement – in contrast to the nanolasers discussed in this chapter, where the photonic modes are utilized. In addition, even though achieving short carrier lifetimes through large Purcell factors is desirable for increasing direct modulation rates, it can have detrimental effects on the optical or electrical injection levels required to achieve transparency and overcome losses [52]. This combination poses interesting challenges for practical implementation of extremely small CW coherent sources operating at room temperature. With this in mind, future research directions in the area of metallo-dielectric nanolasers include electrically pumped coaxial geometry devices, integration of nanolasers with silicon-on-insulator chip-scale waveguides, and gain material grown radially around a nanowire core. Theoretical analysis employing rate equations and the linewidth behavior of 3D nanolasers are also topics of great interest and importance.

Acknowledgments

The authors would like to acknowledge the support from the Defense Advanced Research Projects Agency (DARPA), the National Science Foundation (NSF), the NSF Center for Integrated Access Networks (CIAN), the Cymer Corporation, and the US Army Research Office.

References

1. McCall, S.L., Levi, A.F.J., Slusher, R.E., Pearton, S.J., and Logan, R.A. (1992) Whispering-gallery mode microdisk lasers. *Appl. Phys. Lett.*, **60**, 289–291.
2. Jin Shan, P., Po Hsiu, C., Tsin Dong, L., Yinchieh, L., and Kuochou, T. (1998) 0.66 μm InGaP/InGaAlP single quantum well microdisk lasers. *Jpn. J. Appl. Phys., Part 2*, **37**, L643–L645.
3. Md Zain, A.R., Johnson, N.P., Sorel, M., and De La Rue, R.M. (2009) High quality-factor 1-D-suspended photonic crystal/photonic wire silicon waveguide microcavities. *IEEE Photon. Technol. Lett.*, **21**, 1789–1791.
4. Akahane, Y., Asano, T., Song, B.S., and Noda, S. (2003) High-Q photonic nanocavity in a two-dimensional photonic crystal. *Nature*, **425**, 944–947.
5. Song, Q., Cao, H., Ho, S.T., and Solomon, G.S. (2009) Near-IR sub-wavelength microdisk lasers. *Appl. Phys. Lett.*, **94**, 061109.
6. Smotrova, E.I., Nosich, A.I., Benson, T.M., and Sewell, P. (2006) Optical coupling of whispering-gallery modes of two identical microdisks and its effect on photonic molecule lasing. *IEEE J. Sel. Top. Quantum Electron.*, **12**, 78–85.
7. Nezhad, M.P., Simic, A., Bondarenko, O., Slutsky, B., Mizrahi, A., Feng, L., Lomakin, V., and Fainman, Y. (2010) Room-temperature subwavelength metallo-dielectric lasers. *Nat. Photonics*, **4**, 395–399.
8. Nezhad, M.P., Tetz, K., and Fainman, Y. (2004) Gain assisted propagation of surface plasmon polaritons on planar metallic waveguides. *Opt. Express*, **12**, 4072–4079.
9. Hill, M.T. *et al.* (2007) Lasing in metallic-coated nanocavities. *Nat. Photonics*, **1**, 589–594.
10. Johnson, P.B. and Christy, R.W. (1972) Optical constants of the noble metals. *Phys. Rev. B*, **6**, 4370–4379.

11. Goebel, E.O., Luz, G., and Schlosser, E. (1979) Optical gain spectra of InGaAsP–InP double heterostructures. *IEEE J. Quantum Electron.*, **15**, 697–700.
12. Korbl, M., Groning, A., Schweizer, H., and Gentner, J.L. (2002) Gain spectra of coupled InGaAsP/InP quantum wells measured with a segmented contact traveling wave device. *J. Appl. Phys.*, **92**, 2942–2944.
13. Hill, M.T. *et al.* (2009) Lasing in metal–insulator–metal sub-wavelength plasmonic waveguides. *Opt. Express*, **17**, 11107–11112.
14. Mizrahi, A., Lomakin, V., Slutsky, B.A., Nezhad, M.P., Feng, L., and Fainman, Y. (2008) Low threshold gain metal coated laser nanoresonators. *Opt. Lett.*, **33**, 1261–1263.
15. Lee, J.H., Khajavikhan, M., Simic, A., Gu, Q., Bondarenko, O., Slutsky, B., Nezhad, M.P., and Fainman, Y. (2011) Electrically pumped sub-wavelength metallo-dielectric pedestal pillar lasers. *Opt. Express*, **19** (22), 21524–21531.
16. Bondarenko, O., Simic, A., Gu, Q., Lee, J.H., Slutsky, B., Nezhad, M.P., and Fainman, Y. (2011) Wafer bonded sub-wavelength metallo-dielectric laser. *IEEE Photonics J.*, **3** (3), 608–616.
17. Ding, Q., Mizrahi, A., Fainman, Y., and Lomakin, V. (2011) Dielectric shielded nanoscale patch resonators. *Opt. Lett.*, **36**, 1812–1814.
18. Khajavikhan, M., Simic, A., Katz, M., Lee, J.H., Slutsky, B., Mizrahi, A., Lomakin, V., and Fainman, Y. (2012) Thresholdless nanoscale coaxial lasers. *Nature*, **482** (7384), 204–207.
19. Yeh, P., Yariv, A., and Marom, E. (1978) Theory of Bragg fiber. *J. Opt. Soc. Am.*, **68**, 1196.
20. Mizrahi, A. and Schächter, L. (2004) Bragg reflection waveguides with a matching layer. *Opt. Express*, **12**, 3156.
21. Miyagi, M., Hongo, A., and Kawakami, S. (1983) Transmission characteristics of dielectric-coated metallic waveguide for infrared transmission: slab waveguide model. *IEEE J. Quantum Electron.*, **19**, 136.
22. Smotrova, A.E.I. and Nosich, A.I. (2004) Mathematical study of the two-dimensional lasing problem for the whispering-gallery modes in a circular dielectric microcavity. *Opt. Quantum Electron.*, **36**, 213.
23. Palik, E.D. (1985) *Handbook of Optical Constants of Solids*, Academic Press.
24. Novotny, L. and Hafner, C. (1994) Light propagation in a cylindrical waveguide with a complex, metallic, dielectric function. *Phys. Rev. E.*, **50**, 4094.
25. Baba, T. (1997) Photonic crystals and microdisk cavities based on GaInAsP–InP system. *IEEE J. Sel. Top. Quantum Electron.*, **3**, 808–830.
26. Baba, T., Fujita, M., Sakai, A., Kihara, M., and Watanabe, R. (1997) Lasing characteristics of GaInAsP–InP strained quantum-well microdisk injection lasers with diameter of 2–10 μm . *IEEE Photonics Technol. Lett.*, **9**, 878–880.
27. Asada, M. and Suematsu, Y. (1985) Density-matrix theory of semiconductor lasers with relaxation broadening model-gain and gain-suppression in semiconductor lasers. *IEEE J. Quantum Electron.*, **21**, 434–442.
28. Liu, Z., Shainline, J.M., Fernandes, G.E., Xu, J., Chen, J., and Gmachl, C.F. (2010) Continuous-wave subwavelength microdisk lasers at $\lambda = 1.53 \mu\text{m}$. *Opt. Express*, **18**, 19242–19248.
29. Van Campenhout, J., Rojo-Romeo, P., Van Thourhout, D., Seassal, C., Regreny, P., Cioccio, L.D., Fedeli, J.-M., and Baets, R. (2007) Thermal characterization of electrically injected thin-film InGaAsP microdisk lasers on Si. *J. Lightwave Technol.*, **25**, 1543–1548.
30. Albert, F., Braun, T., Heindel, T., Schnedier, C., Reitzenstein, S., Höfling, S., Worschech, L., and Forchel, A. (2010) Whispering gallery mode lasing in electrically driven quantum dot micropillars. *Appl. Phys. Lett.*, **97**, 101108.
31. Purcell, E.M. (1946) Spontaneous emission probabilities at radio frequencies. *Phys. Rev.*, **69**, 681.
32. Berman, P. (ed.) (1994) *Cavity Quantum Electrodynamics*, Academic Press, San Diego, CA.
33. Abe, H., Furumoto, T., Narimatsu, M., Kita, S., Nakamura, K., Takemura, Y., and Baba, T. (2012) Direct live cell imaging using large-scale nanolaser array. *IEEE Sens.*, **1565**, 4.

34. Ma, R.-M., Yin, X., Oulton, R.F., Sorger, V.J., and Zhang, X. (2012) Multiplexed and electrically modulated plasmon laser circuit. *Nano Lett.*, **12**, 5396–5402.
35. Noda, S. (2006) Seeking the ultimate nanolasers. *Science*, **314** (5797), 260–261.
36. Burgos, S.P., deWaele, R., Polman, A., and Atwater, H.A. (2010) A single-layer wide-angle negative-index metamaterial at visible frequencies. *Nat. Mater.*, **9**, 407–412.
37. Jacob, Z. and Shalae, V.M. (2011) Plasmonics goes quantum. *Science*, **28**, 463.
38. Yokoyama, H. (1992) Physics and device applications of optical microcavities. *Science*, **256** (5053), 66–70.
39. Bjork, G. and Yamamoto, Y. (1991) Analysis of semiconductor microcavity lasers using rate equations. *IEEE J. Quantum Electron.*, **27**, 2386–2396.
40. Baida, F.I., Belkhir, A., and Van Labeke, D. (2006) Subwavelength metallic coaxial waveguides in the optical range: role of the plasmonic modes. *Phys. Rev. B*, **74**, 205419.
41. Feigenbaum, E. and Orenstein, M. (2008) Ultrasmall volume plasmons, yet with complete retardation effects. *Phys. Rev. Lett.*, **101** (16), 163902.
42. Benzaquen, R. *et al.* (1994) Alloy broadening in photoluminescence spectra of $\text{Ga}_x\text{In}_{1-x}\text{As}_y\text{P}_{1-y}$ lattice matched to InP. *J. Appl. Phys.*, **75** (5), 2633–2639.
43. Bayer, M. *et al.* (2001) Inhibition and enhancement of the spontaneous emission of quantum dots in structured microresonators. *Phys. Rev. Lett.*, **86** (14), 3168–3171.
44. Vuckovic, J., Painter, O., Xu, Y., Yariv, A., and Scherer, A. (1999) Finite-difference time-domain calculation of the spontaneous emission coupling factor in optical microcavities. *IEEE J. Quantum Electron.*, **35**, 1168.
45. Schawlow, A.L. and Townes, C.H. (1958) Infrared and optical masers. *Phys. Rev.*, **112** (6), 1940.
46. Henry, C. (1982) Theory of the linewidth of semiconductor lasers. *IEEE J. Quantum Electron.*, **18** (2), 259–264.
47. Björk, G., Karlsson, A., and Yamamoto, Y. (1992) On the linewidth of microcavity lasers. *Appl. Phys. Lett.*, **60**, 304.
48. Rice, P.R. and Carmichael, H.J. (1994) Photon statistics of a cavity-QED laser: a comment on the laser-phase-transition analogy. *Phys. Rev. A*, **50** (5), 4318–4329.
49. Pedrotti, L.M., Sokol, M., and Rice, P.R. (1999) Linewidth of four-level microcavity lasers. *Phys. Rev. A*, **59**, 2295.
50. Roy-Choudhury, K. and Levi, A.F.J. (2011) Quantum fluctuations and saturable absorption in mesoscale lasers. *Phys. Rev. A*, **83**, 043827.
51. Strauf, S. *et al.* (2006) Self-tuned quantum dot gain in photonic crystal lasers. *Phys. Rev. Lett.*, **96** (12), 127404/1–127404/4.
52. Khurgin, J.B. and Sun, G. (2012) Practicality of compensating the loss in the plasmonic waveguides using semiconductor gain medium. *Appl. Phys. Lett.*, **100** (1), 011105.

